GEOLOGY | THE GEOLOGICAL SOCIETY OF AMERICA®

https://doi.org/10.1130/G47656.1

Manuscript received 25 March 2020
Revised manuscript received 9 June 2020
Manuscript accepted 11 June 2020

Published online XX Month 2020

Flank sliding: A valve and a sentinel for paroxysmal eruptions and magma ascent at Mount Etna, Italy

Giuseppe Pezzo[1], Mimmo Palano[2], Cristiano Tolomei[1], Pasquale De Gori[1], Stefano Calcaterra[3], Piera Gambino[3] and Claudio Chiarabba[1]

[1]Istituto Nazionale di Geofisica e Vulcanologia, Osservatorio Nazionale Terremoti, Rome 00143, Italy
[2]Istituto Nazionale di Geofisica e Vulcanologia, Sezione di Catania, Osservatorio Etneo, Catania 95125, Italy
[3]Italian Institute for Environmental Protection and Research (ISPRA), Rome 00144, Italy

ABSTRACT

Rising magma, dike intrusions, and flank collapse are observed at many volcanoes worldwide, but how they interact is still poorly documented. Extensive synthetic aperture radar interferometry and continuous global positioning system observations captured a sharp dike intrusion at Mount Etna, Italy, during the 2018 paroxysm that triggered a vigorous seaward sliding of the eastern flank connected with brittle failure and deep magmatic resourcing. We propose a feedback process between flank acceleration and magma intrusion that derives from the interaction between the long- and short-term deformation of the volcano. The flank sliding acts as a valve that modulates the emplacement and eruption of magma within the shallow system. Rapid flank acceleration could potentially evolve into sudden collapses and seismic release at shallow depth. In turn, flank slip events could act as a sentinel for changes in magma depth and paroxysmal eruptions at Mount Etna.

INTRODUCTION

The pressurization of magmatic bodies and intrusions through the shallow crust influence the local stress state, promoting fault slip and movements of unstable volcano flanks (Savage and Clark, 1982; Sigmundsson et al., 1997; Cayol et al., 2000; Hill et al., 2002; Walter et al., 2005). Mechanisms of dike propagation and interaction with preexisting structures are highly debated (Rubin, 1995; Valentine and Krogh, 2006; Acocella and Neri, 2009; Maccaferri et al., 2015; Rivalta et al., 2015), because they might influence the magma emplacement and flank instability, as inferred for Krakatau (Indonesia; Deplus et al., 1995), Kilauea (Hawaii, USA; Neal et al., 2019), Stromboli (Italy; Tibaldi et al., 2003), and Mount Etna (Italy; Tibaldi and Groppelli, 2002; Carbone et al., 2009; Urlaub et al., 2018).

The vivid dynamics of Mount Etna enable evolutionary processes to be captured within relatively short time periods, providing key information and lessons for other volcanoes worldwide. Large-scale seaward motion of the eastern flank of Mount Etna has been documented since the early 1990s (Borgia et al., 1992; Branca and Ferrara, 2013; Urlaub et al., 2018), as well as the interaction between the flank motion and eruptions (e.g., Acocella et al., 2003; Walter et al., 2005).

During the few days of the December 2018 paroxysm, we observed (1) the intrusion of a dike on 24 December (see Figs. 1A–1C); (2) a large shallow earthquake on 26 December (Mw 4.9; Figs. 1C and 1D) along the Fiandaca fault, an arcuate fault running on the eastern flank of the volcano (Azzaro et al., 2013); (3) lava emission from the eruptive fractures in the upper eastern sector of the volcano between 24 and 27 December; and (4) post-event acceleration of flank sliding coupled with pressurization of a deep reservoir.

Using a large data set, including continuous global positioning system (CGPS) and synthetic aperture radar interferometry (InSAR) data, we set constraints on the processes leading to the dike intrusion and to the earthquake. We also present the first continuous measurement of the flank acceleration following an intrusion, as captured by CGPS and multitemporal InSAR time series. Finally, we integrated deformation source models deduced from the Coulomb failure function (CFF) and tomographic models (Giampiccolo et al., 2020) to obtain a comprehensive view of the volcano's dynamic processes.

DATA AND METHODS

CGPS observations collected during the 1 December 2018–28 June 2019 time span were analyzed using the GAMIT/GLOBK software (http://geoweb.mit.edu/gg/; Herring et al., 2018); daily time series and displacements (Figs. 1E and 1F) were referred to a local reference frame (Palano et al., 2017). In order to constrain the temporal evolution of the events, we computed the high-rate solutions of selected CGPS stations using the TRACK software (http://geoweb.mit.edu/gg/; Herring et al., 2018; see the Supplemental Material[1]).

Using Sarscape software (http://www.sarmap.ch/wp/index.php/software/sarscape/), we processed a SAR data set consisting of two C-band *Sentinel-1* (European Space Agency) pairs, in ascending and descending geometry (22–28 December; Figs. 2A and 2B), and a descending L-band *ALOS-2* (Japan Aerospace Exploration Agency) pair (18 December–29 January; Fig. 2C). Corresponding displacement maps are shown in Figures 2D, 2E, and 2F. To capture the post-event deformation (Fig. 3), we processed 29 descending (December 2018 through June 2019) and 29 ascending (January 2019 through June 2019) SAR *Sentinel-1* images using the small baseline subset (SBAS) approach (Berardino et al., 2002). We applied multilooking factors of 6 and 23 for the azimuth and range directions to obtain a ground resolution of 90 m.

[1]Supplemental Material. Description of the volcanic and seismic activity at Mount Etna, and details on the data processing and models. Please visit https://doi.org/10.1130/~~XXXXX~~1 to access the supplemental material, and contact editing@geosociety.org with any questions.

CITATION: Pezzo, G., et al., 2020, Flank sliding: A valve and a sentinel for paroxysmal eruptions and magma ascent at Mount Etna, Italy: Geology, v. 48, p. XXX–XXX, https://doi.org/10.1130/G47656.1

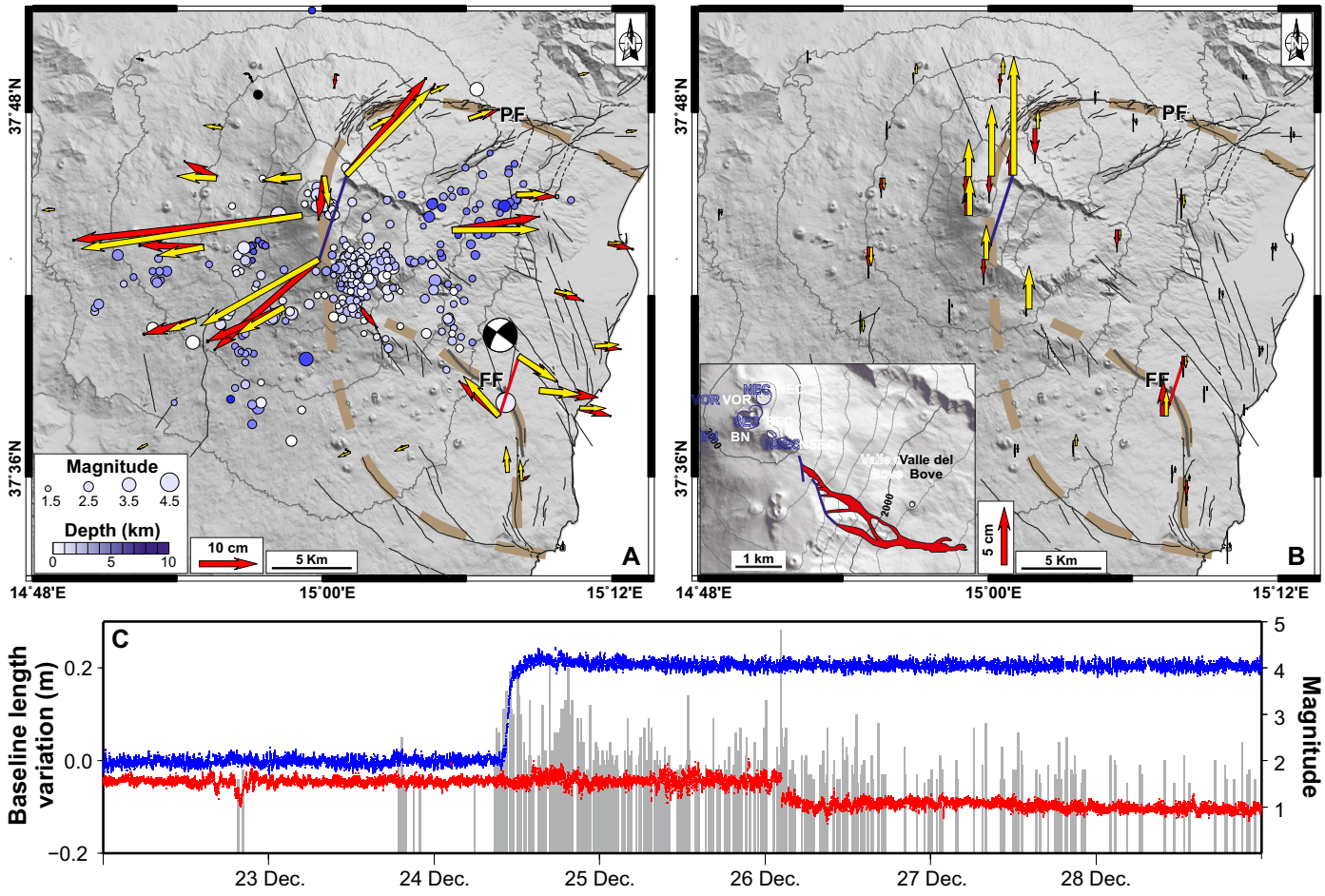

Figure 1. Map of Mount Etna, Italy, showing December 2018 eruption. (A) Horizontal observed (red) and modeled (yellow) ground deformations covering the 22–28 December 2018 period. Seismicity and M 4.9 earthquake focal mechanism (http://cnt.rm.ingv.it/event/21285011#) are plotted. Green dotted line marks boundary of the unstable flank (FF—Fiandaca fault; PF—Pernicana fault). Red and blue lines indicate baselines reported in C. (B) Vertical observed (red) and modeled (yellow) ground deformations covering same period. Inset shows Mount Etna summit area with eruptive fracture field (blue lines) opened on 24 December, and emitted lava. NEC—North-East crater; VOR—Voragine; BN—Bocca Nuova; SEC—South-East crater, NSEC—New South-East crater. (C) High-rate baseline length variations for selected couples of continuous global positioning system (CGPS) stations located close to the summit area (blue) and across the Fiandaca fault (red).

Double filtering in space and time (high and low band-pass) was applied to remove atmospheric artifacts. For both single-pair and multitemporal SAR processing, we used the 30-m-resolution Shuttle Radar Topography Mission digital elevation model for the topography subtraction step.

CGPS and SAR data sets were jointly inverted to obtain the dike opening and fault slip models, while we used CGPS measurements to invert the short-term dike evolution and the post-intrusion inflation pattern.

The joint inversion was performed using Okada's (1985) formalism for the dike and fault sources, after separating their relative contributions to the ground deformation. We adopted a two-step approach (Atzori et al., 2009) consisting of a nonlinear inversion for the location, dimension, and orientation of a homogeneous dike opening, followed by a linear inversion for the opening distribution along the plane. Nonlinear-inversion parameter uncertainties and trade-offs show how positions and orientation are well constrained, with an opening distribution uncertainty <4.3 cm and a resolution varying from 250 m at the surface to 1.3 km at depths >3 km below sea level (bsl). To model the fault slip, we directly performed a linear inversion, constraining the fault geometry and rake from interferogram fringe patterns and the focal mechanism (Fig. 2).

The evolution of the intrusive event was modeled by performing day-by-day inversions of CGPS displacements (Fig. 4B), keeping the previously defined dike geometry fixed. We also modeled the post-event ground deformation (Fig. 3A), adopting the Yang et al. (1988) formalism.

In order to investigate how the dike opening affected faults and flank sliding, we estimated the static stress changes through the CFF approach. We set the dike opening distribution as the stress source, whereas the Fiandaca fault and the detachment plane, on which the Fiandaca fault soles, were the receivers. The detachment was assumed to be located at the volcanic-sedimentary interface (Palano, 2016) with the geometry constrained by the isovelocity surface in tomographic models (Giampiccolo et al., 2020), in agreement with geologic data (Branca and Ferrara, 2013) and the shallow slip observed on the Fiandaca fault.

Additional details on modeling methods and parameter uncertainties are given in the Supplemental Material.

RESULTS

Co-event CGPS and InSAR ground deformation patterns (Figs. 2D, 2E, and 2F) were dominated by a roughly 1 m ENE-WSW–oriented widening of the volcano. After the 24 December intrusion, the northern portion of the flank began to creep, while the southern portion remained locked until the Mw 4.9 strike-slip earthquake on 26 December (Figs. 1C and 3D). CGPS and InSAR data coherently detected a post-event acceleration of the eastern flank, speeding up to 15 cm/yr (Fig. 3) from the average rate of 3.3–6.1 cm/yr (Palano, 2016). Aseismic creep occurs along a detachment surface and a set

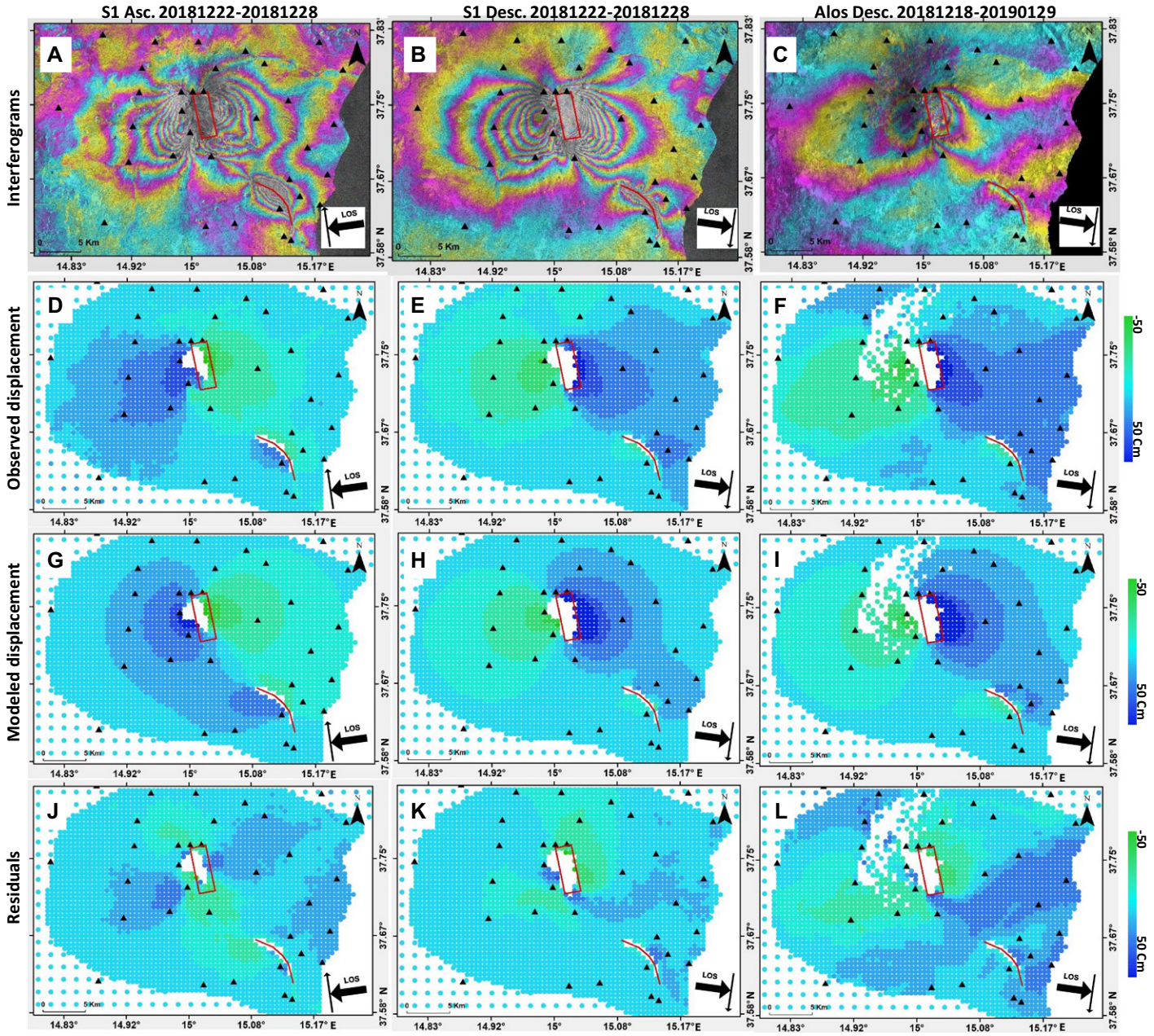

Figure 2. (A–B) *Sentinel-1* (European Space Agency) ascending (A) and descending (B) interferograms covering 22–28 December 2018 period. (C) *ALOS-2* (Japan Aerospace Exploration Agency) descending interferogram, spanning 18 December 2018 to 29 January 2019. (D–F) Corresponding subsampled displacement maps. (G–I) Modeled displacement maps for three data sets. (J–L) Residuals for three data sets. Blue colors (positive values) are approaching sensor; green colors (negative displacements) are moving away along satellite lines of sight (LOS), sketched as black arrows orthogonal to flight paths. Red box and segments represent surface dike projection and fault trace, respectively. Black triangles are continuous global positioning system (CGPS) benchmarks.

of edge faults (e.g., the Pernicana to the north and the Fiandaca to the south). In addition, the post-event ground deformation pattern identified a near-radial inflation (Fig. 3A; Table S1 in the Supplemental Material) that summed up to the long-term steady inflation of the volcano (Fig. 3C).

The main observed deformation is consistent with the opening of a NNW-SSE–oriented, 68°E-dipping dike with a tensile component up to ~3 m in its upper portion (from 1000 m above sea level [asl] to the top; Fig. 4A). The short-term evolution during the period 23–28 December highlights a progressive downdip opening of the dike (from $z > 1800$ m asl on 23–24 December to $z < 1800$ m on 24–25 and 25–28 December; see Fig. 4).

The fault model consists of an arcuate four-segment fault with a maximum slip of ~1 m confined within the upper 2 km of the fault (Fig. 4A), suggesting that flank sliding is accommodated by shallow faults at the edges, which sole into the detachment plane.

The post-intrusion deformation is consistent with the inflation of a magmatic reservoir located at a depth of 6.5 km bsl beneath the summit area, showing a positive volume variation of 15.7×10^6 m^3 (see Fig. 3).

Results of CFF analysis showed a maximum stress increase of 0.16 MPa on the fault induced by the dike opening and a maximum of ~100 MPa on the upper portion of the detachment plane (Fig. 4C). We also evaluated how the sliding of the flank interacted with the dike intrusion, calculating the pressure variation along a vertical profile beneath the summit area caused by the long-term sliding and by the post-intrusion acceleration. Assuming a rigid, steady movement of the collapsing block

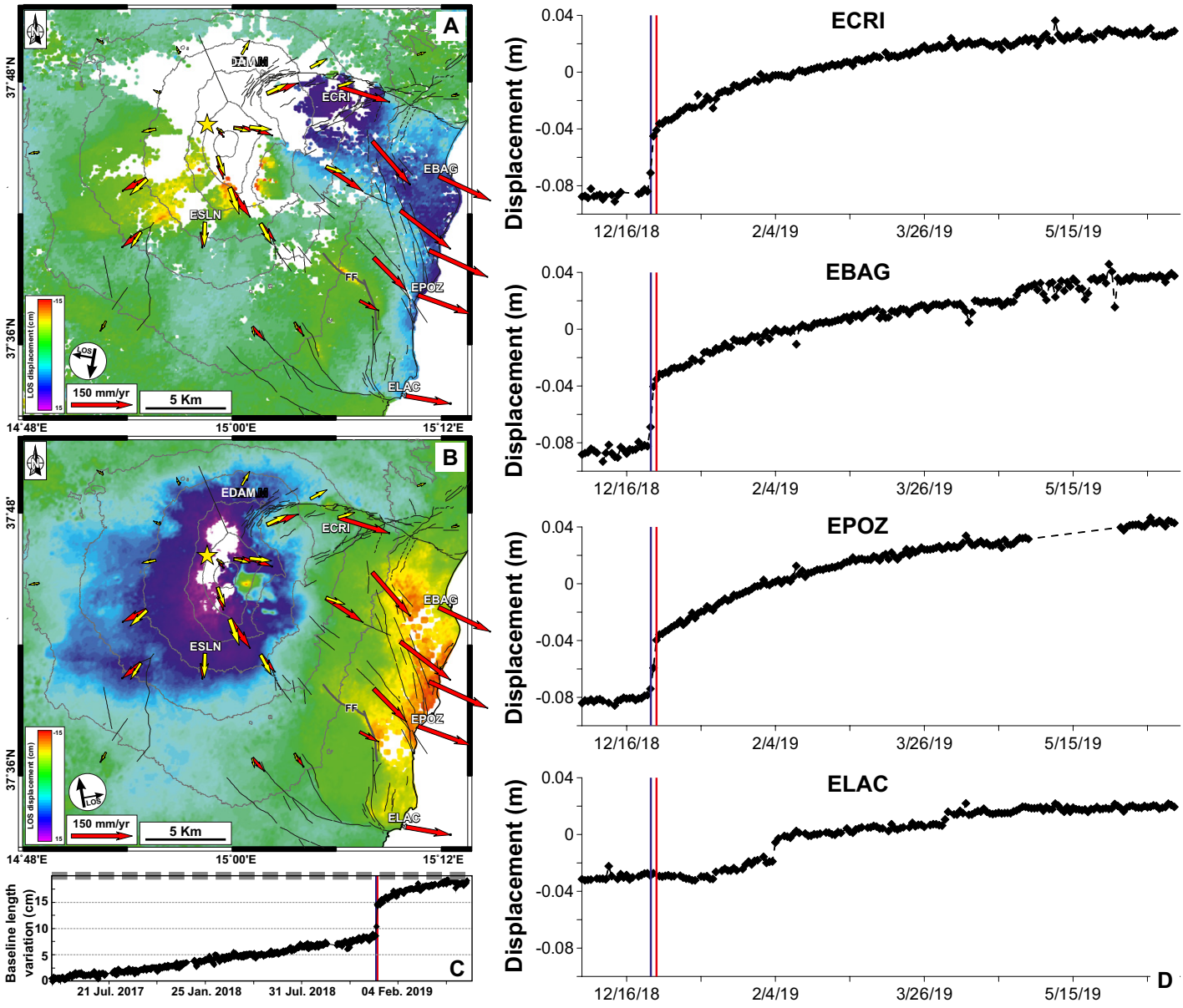

Figure 3. (A) *Sentinel-1* (European Space Agency) mean velocity map in descending synthetic aperture radar (SAR) geometry covering 28 December 2018 to 20 June 2019 time window. Blue colors (positive values) are approaching the sensor; red colors (negative velocities) are moving away along line of sight (LOS). Red (observed) and yellow (modeled) arrows represent horizontal continuous global positioning system (CGPS) velocities in the same time span. Yellow star represents surface projection of modeled source (see Table S1 in the Supplemental Material [see footnote 1]). EDAM, ESLN, ECRI, EBAG, EPOZ and ELAC are CGPS stations. Main faults are also shown on the map (FF—Fiandaca fault). (B) *Sentinel-1* mean velocity map in ascending geometry covering 3 January 2019 to 26 June 2019 time window. (C) Length variation of EDAM-ESLN baseline during 1 April 2017 to 26 June 2019 period. (D) Example of time series of east component of four CGPS stations. In C and D, blue and red vertical lines mark the start of eruption and the M 4.9 earthquake occurrence, respectively.

at 4.5 cm/yr, we inferred a pressure decrease of ~1 MPa/yr in the upper portion of the volcano, 1.4 km from the top (Fig. 4D). Considering a post-intrusion acceleration up to 15 cm/yr velocity, we obtained a similar pattern but with values up to 3 MPa/yr (profiles in Fig. 4D).

DISCUSSION AND CONCLUSIONS

Previous models of the 2018 intrusive event, constrained by the *Sentinel-1* SAR pairs, consist of a vertically linked, three-source asset, with two dikes and a deep deflation (Bonforte et al., 2019) or a double-source system with partially overlapping dikes (De Novellis et al., 2019). Our model results in a simplified dike geometry, but it captures all the key features and the evolution of the intrusion. The day-by-day opening distribution along the dike (Fig. 4B) suggests that the eruption was initially fed by magma stored at shallow levels, and later by deeper magma. The model predicts an uplift in the volcano summit area that was not seen by CGPS stations; this discrepancy may be due to a lack of compensation between the lava withdrawal by the eruption and deeper magma supply or, more likely, to an oversimplification of the elastic medium in modeling.

The dike intrusion yielded a dramatic stress increase on the detachment plane, promoting the flank sliding acceleration (up to 15 cm/yr) and the occasional brittle failure on faults at the collapse edge. In turn, the flank sliding favored the remobilization of magma residing at shallow depth and the cessation of the eruption for the sudden depressurization at the dike top, like a one-way valve (Figs. 4C and 4D, step 2). The shallow dike emplacement and eruption were followed by a deeper intrusion below the detachment surface (Fig. 4B), coupled with a deep re-filling of the system and the acceleration of flank sliding (Fig. 4D).

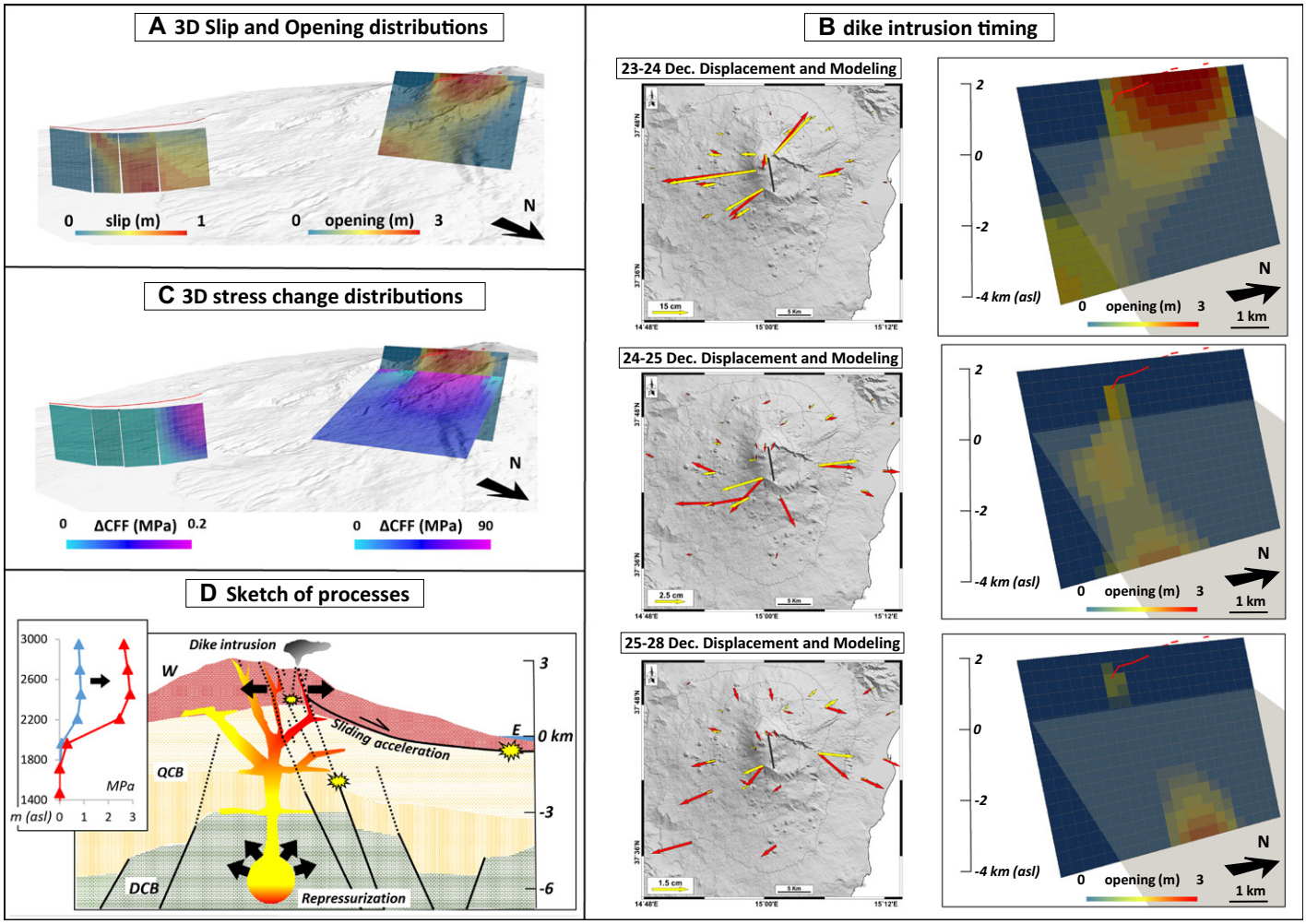

Figure 4. (A) Three-dimensional (3-D) northeast view of slip and opening distribution along a modeled fault and dike. (B) Timing of dike intrusion obtained by inversions of continuous global positioning system (CGPS) ground displacement fields in three steps, during 23–28 December 2018; red and yellow arrows are observed and modeled CGPS displacement, respectively; black line is surface trace of modeled dike. On right: dike opening distributions and sliding plane (in transparent gray; asl—above sea level). (C) Three-dimensional northeast view of static stress variations (Coulomb failure function difference [ΔCFF]) induced by dike intrusion on the 26 December fault and sliding plane of the volcano flank collapse. Positive values (up to 90 Mpa) favor failure (from cyan to purple); negative values represent stress release. (D) Cartoon of feedback process; QCB—Quaternary clay basement; DCB—deep carbonate basement. Inset represents depressurization vertical profiles due to flank sliding, back to sliding plane.

We hypothesize that magma ascent is favored by weak zones within the sedimentary basement, identified by a sharp E-dipping scarp in tomographic models, lying in vertical continuity with the modeled dike. The 2018 dike is part of a set of coalescing structures, which form the shallow rifting system involved in recent eruptions (e.g., 1997, 2001, 2002–2003, and 2008; Aloisi et al., 2009; Palano et al., 2017). During the 2002–2003 eruption, seismicity developed along the south and the northeast rift zones, heralding the dike intrusions and eruption, coupled with a sudden sliding of the northern sector of the flank and the occurrence of three M > 4.2 shallow earthquakes at its southern edge (e.g., Barberi et al., 2004).

The interaction between gravitational phenomena and rising magma, potentially channeled through preexisting weak zones, controls the stratovolcano construction, evolution, and dynamics. Previous models hypothesized that the eastern flank collapse is driven by magma pushing along the central conduits that mobilize a deep E-verging thrust fault (Walter et al., 2005). Conversely, in our model, the push of the rising magma acts on a shallow E-dipping detachment located at the volcano-sedimentary interface. This shallow depth of the detachment is consistent with the very surficial slip observed on the edge faults (like the Fiandaca fault) and the modeling of GPS data (Palano, 2016). While a long-term steady sliding induces a progressive depressurization (1 MPa/yr) of the shallow system, occasional post-eruptive flank sliding accelerations are linked to deep magma pressurization. Repetition over time of this process produces a long-term instability of the flank that acts as a valve in remobilizing shallow magma, but an abrupt catastrophic collapse of the flank might be coupled with fast ascent of deep magma, leading to paroxysmal eruptions. Complementary, abrupt accelerations of flank sliding could be considered a sentinel for post-event deep resourcing of the magma reservoir. In any case, such powerful data sets still do not allow short transient signals (hours to days) related to magma pushing to be captured, nor related to deep repressurization and transit of magma from the mantle source.

Large data sets from Mount Etna highlight processes occurring over different temporal and spatial scales, thus providing knowledge that can be used to study other volcanoes. Interactions among flank slip events, changes in the depth of magma, and eruption frequency appear to be episodic also at Kilauea, as documented by the 2018 lower East Rift Zone eruption (Neal et al., 2019). In that particular case, continued withdrawal of magma resulted in the collapse of the volcano edifice, channeled by preexisting

crustal weaknesses, including the caldera ring-fault system (Anderson et al., 2019). The open question of whether the reduction of summit magma pressure due to flank sliding could promote a new magma supply from depth seems to be confirmed in the case of Mount Etna.

ACKNOWLEDGMENTS

We thank S. Atzori for supporting the data inversions, and G. Puglisi and C. Doglioni for fruitful discussions. We also thank Daniele Pellegrino, Mario Pulvirenti, and Massimo Rossi, technicians of the INGV, who ensured the regular working of the CGPS stations at Mount Etna. We thank the editor and the reviewers for their useful comments. *Sentinel-1* and *ALOS-2* data used here with permission are copyrighted by Copernicus (European Union) and the Japan Aerospace Exploration Agency (JAXA), respectively.

REFERENCES CITED

Acocella, V., and Neri, M., 2009, Dike propagation in volcanic edifices: Overview and possible developments: Tectonophysics, v. 471, p. 67–77, https://doi.org/10.1016/j.tecto.2008.10.002.

Acocella, V., Behncke, B., Neri, M., and D'Amico, S., 2003, Link between major flank slip and 2002–2003 eruption at Mt. Etna (Italy): Geophysical Research Letters, v. 30, 2286, https://doi.org/10.1029/2003GL018642.

Aloisi, M., Bonaccorso, A., Cannavò, F., Gambino, S., Mattia, M., Puglisi, G., and Boschi, E., 2009, A new dyke intrusion style for the Mount Etna May 2008 eruption modelled through continuous tilt and GPS data: Terra Nova, v. 21, p. 316–321, https://doi.org/10.1111/j.1365-3121.2009.00889.x.

Anderson, K.R., Johanson, I.A., Patrick, M.R., Gu, M., Segall, P., Poland, M.P., Montgomery-Brown, E.K., and Miklius, A., 2019, Magma reservoir failure and the onset of caldera collapse at Kīlauea Volcano in 2018: Science, v. 366, p. 1214, https://doi.org/10.1126/science.aaz1822.

Atzori, S., et al., 2009, Finite fault inversion of DInSAR coseismic displacement of the 2009 L'Aquila earthquake (central Italy): Geophysical Research Letters, v. 36, L15305, https://doi.org/10.1029/2009GL039293.

Azzaro, R., D'Amico, S., Peruzza, L., and Tuvè, T., 2013, Probabilistic seismic hazard at Mt. Etna (Italy): The contribution of local fault activity in mid-term assessment: Journal of Volcanology and Geothermal Research, v. 251, p. 158–169, https://doi.org/10.1016/j.jvolgeores.2012.06.005.

Barberi, G., Cocina, O., Maiolino, V., Musumeci, C., and Privitera, E., 2004, Insight into Mt. Etna (Italy) kinematics during the 2002-2003 eruption as inferred from seismic stress and strain tensors: Geophysical Research Letters, v. 31, L21614, https://doi.org/10.1029/2004GL020918.

Berardino, P., Fornaro, G., Lanari, R., and Sansosti, E., 2002, A new algorithm for surface deformation monitoring based on small baseline differential SAR interferograms: IEEE Transactions on Geoscience and Remote Sensing, v. 40, p. 2375–2383, https://doi.org/10.1109/TGRS.2002.803792.

Bonforte, A., Guglielmino, F., and Puglisi, G., 2019, Large dyke intrusion and small eruption: The December 24, 2018, Mt. Etna eruption imaged by *Sentinel-1* data: Terra Nova, v. 31, p. 405–412, https://doi.org/10.1111/ter.12403.

Borgia, A., Ferrari, L., and Pasquarè, G., 1992, Importance of gravitational spreading in the tectonic and volcanic evolution of Mount Etna: Nature, v. 357, p. 231–235, https://doi.org/10.1038/357231a0.

Branca, S., and Ferrara, V., 2013, The morphostructural setting of Mount Etna sedimentary basement (Italy): Implications for the geometry and volume of the volcano and its flank instability: Tectonophysics, v. 586, p. 46–64, https://doi.org/10.1016/j.tecto.2012.11.011.

Carbone, D., D'Amico, S., Musumeci, C., and Greco, F., 2009, Comparison between the 1994–2006 seismic and gravity data from Mt. Etna: New insight into the long-term behavior of a complex volcano: Earth and Planetary Science Letters, v. 279, p. 282–292, https://doi.org/10.1016/j.epsl.2009.01.007.

Cayol, V., Dieterich, J.H., Okamura, A.T., and Miklius, A., 2000, High magma storage rates before the 1983 eruption of Kilauea, Hawaii: Science, v. 288, p. 2343–2346, https://doi.org/10.1126/science.288.5475.2343.

De Novellis, V., et al., 2019, DInSAR analysis and analytical modelling of Mt. Etna displacements: The December 2018 volcano-tectonic crisis: Geophysical Research Letters, v. 46, p. 5817–5827, https://doi.org/10.1029/2019GL082467.

Deplus, C., Bonvalot, S., Dahrin, D., Diament, M., Harjono, H., and Dubois, J., 1995, Inner structure of the Krakatau volcanic complex (Indonesia) from gravity and bathymetry data: Journal of Volcanology and Geothermal Research, v. 64, p. 23–52, https://doi.org/10.1016/0377-0273(94)00038-I.

Giampiccolo, E., Cocina, O., De Gori, P., and Chiarabba, C., 2020, Dyke intrusion and stress-induced collapse of volcano flanks: The example of the 2018 event at Mt. Etna: Nature Scientific Reports, v. 10, p. 6373, https://doi.org/10.1038/s41598-020-63371-3.

Herring, T.A., King, R.W., Floyd, M.A., and McClusky, S.C., 2018, Introduction to GAMIT/GLOBK, Release 10.70: Cambridge, Massachusetts, Massachusetts Institute of Technology, 54 p.

Hill, D.P., Pollitz, F., and Newhall, C., 2002, Earthquake-volcano interactions: Physics Today, v. 55, p. 41–47, https://doi.org/10.1063/1.1535006.

Maccaferri, F., Acocella, V., and Rivalta, E., 2015, How the differential load induced by normal fault scarps controls the distribution of monogenic volcanism: Geophysical Research Letters, v. 42, p. 7507–7512, https://doi.org/10.1002/2015GL065638.

Neal, C.A., et al., 2019, The 2018 rift eruption and summit collapse of Kīlauea Volcano: Science, v. 363, p. 367–374, https://doi.org/10.1126/science.aav7046.

Okada, Y., 1985, Surface deformation due to shear and tensile faults in a half-space: Bulletin of the Seismological Society of America, v. 75, p. 1135–1154.

Palano, M., 2016, Episodic slow slip events and seaward flank motion at Mt. Etna volcano (Italy): Journal of Volcanology and Geothermal Research, v. 324, p. 8–14, https://doi.org/10.1016/j.jvolgeores.2016.05.010.

Palano, M., Viccaro, M., Zuccarello, F., and Gresta, S., 2017, Magma transport and storage at Mt. Etna (Italy): A review of geodetic and petrological data for the 2002–03, 2004 and 2006 eruptions: Journal of Volcanology and Geothermal Research, v. 347, p. 149–164, https://doi.org/10.1016/j.jvolgeores.2017.09.009.

Rivalta, E., Taisne, B., Bunger, A.P., and Katz, R.F., 2015, A review of mechanical models of dike propagation: Schools of thought, results and future directions: Tectonophysics, v. 638, p. 1–42, https://doi.org/10.1016/j.tecto.2014.10.003.

Rubin, A.M., 1995, Propagation of magma-filled cracks: Annual Review of Earth and Planetary Sciences, v. 23, p. 287–336, https://doi.org/10.1146/annurev.ea.23.050195.001443.

Savage, J.C., and Clark, M.M., 1982, Magmatic resurgence in Long Valley caldera, California: Possible cause of the 1980 Mammoth Lakes earthquakes: Science, v. 217, p. 531–533, https://doi.org/10.1126/science.217.4559.531.

Sigmundsson, F., et al., 1997, The 1994–1995 seismicity and deformation at the Hengill triple junction, Iceland: Triggering of earthquakes by minor magma injection in a zone of horizontal shear stress: Journal of Geophysical Research: Solid Earth, v. 102, no. B7, p. 15151–15161, https://doi.org/10.1029/97JB00892.

Tibaldi, A., and Groppelli, G., 2002, Volcano-tectonic activity along structures of the unstable NE flank of Mt. Etna (Italy) and their possible origin: Journal of Volcanology and Geothermal Research, v. 115, p. 277–302, https://doi.org/10.1016/S0377-0273(01)00305-5.

Tibaldi, A., Corazzato, C., Apuani, T., and Cancelli, A., 2003, Deformation at Stromboli volcano (Italy) revealed by rock mechanics and structural geology: Tectonophysics, v. 361, p. 187–204, https://doi.org/10.1016/S0040-1951(02)00589-9.

Urlaub, M., Petersen, F., Gross, F., Bonforte, A., Puglisi, G., Guglielmino, F., Krastel, S., Lange, D., and Kopp, H., 2018, Gravitational collapse of Mount Etna's southeastern flank: Science Advances, v. 4, p. eaat9700, https://doi.org/10.1126/sciadv.aat9700.

Valentine, G.A., and Krogh, K.E., 2006, Emplacement of shallow dikes and sills beneath a small basaltic volcanic center—The role of pre-existing structure (Paiute Ridge, southern Nevada, USA): Earth and Planetary Science Letters, v. 246, p. 217–230, https://doi.org/10.1016/j.epsl.2006.04.031.

Walter, T.R., Acocella, V., Neri, M., and Amelung, F., 2005, Feedback processes between magmatic events and flank movement at Mount Etna (Italy) during the 2002–2003 eruption: Journal of Geophysical Research: Solid Earth, v. 110, no. B10, B10205, https://doi.org/10.1029/2005JB003688.

Yang, X.M., Davis, P.M., and Dieterich, J.H., 1988, Deformation from inflation of a dipping finite prolate spheroid in an elastic half-space as a model for volcanic stressing: Journal of Geophysical Research, v. 93, p. 4249–4257, https://doi.org/10.1029/JB093iB05p04249.

Printed in USA